

Cell-Type-Specific Metabolic Profiling Achieved by Combining Desorption Electrospray Ionization Mass Spectrometry Imaging and Immunofluorescence Staining

Xin Yan, Xiaoi Zhao, Zhenpeng Zhou, Andrew McKay, Anne Brunet,* and Richard N. Zare*

Cite This: *Anal. Chem.* 2020, 92, 13281–13289

Read Online

ACCESS |



Metrics & More

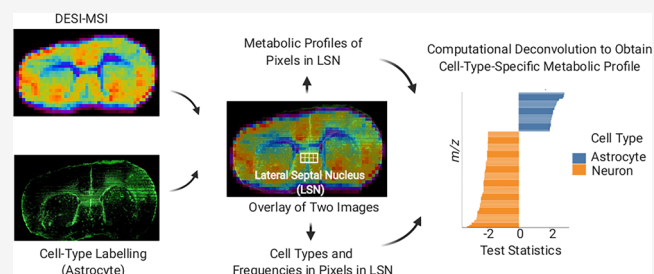


Article Recommendations



Supporting Information

ABSTRACT: Cell-type-specific metabolic profiling in tissue with heterogeneous composition has been of great interest across all mass spectrometry imaging (MSI) technologies. We report here a powerful new chemical imaging capability in desorption electrospray ionization (DESI) MSI, which enables cell-type-specific and *in situ* metabolic profiling in complex tissue samples. We accomplish this by combining DESI-MSI with immunofluorescence staining using specific cell-type markers. We take advantage of the variable frequency of each distinct cell type in the lateral septal nucleus (LSN) region of mouse forebrain. This allows computational deconvolution of the cell-type-specific metabolic profile in neurons and astrocytes by convex optimization—a machine learning method. Based on our approach, we observed 107 metabolites that show different distributions and intensities between astrocytes and neurons. We subsequently identified 23 metabolites using high-resolution mass spectrometry (MS) and tandem MS, which include small metabolites such as adenosine and *N*-acetylaspartate previously associated with astrocytes and neurons, respectively, as well as accumulation of several phospholipid species in neurons which have not been studied before. Overall, this method overcomes the relatively low spatial resolution of DESI-MSI and provides a new platform for *in situ* metabolic investigation at the cell-type level in complex tissue samples with heterogeneous cell-type composition.



The cellular metabolome can be defined as the set of metabolites present in cells, which capitalizes on the small molecules observed to construct a “fingerprint” that can be uniquely assigned to individuals.¹ Metabolome analysis can describe qualitatively and quantitatively the intermediates and products of cellular regulatory pathways.^{2,3} It allows us to understand cell phenotypes and can be seen as the ultimate response of a biologic system to genetic factors and/or environmental changes. Mass spectrometry (MS) plays an increasingly dominant role in the metabolomics field due to its inherent high sensitivity, specificity, and fast data acquisition.^{4–6} Cellular metabolomics has been reported in research for early diagnosis of disease and for understanding the molecular mechanism of disease progression, response, and resistance to therapeutics. It holds promise to inform the practice of precision medicine.^{5,7,8} For example, a number of investigations have been carried out to establish biomarkers for cancers,^{9,10} cardiovascular diseases,^{11,12} neurodegenerative diseases,^{13–15} diabetes,^{16,17} and obesity.¹⁸ However, these studies all employed classic bulk “bind and grind” methods and conventional MS requiring cell homogenates either from tissue or cell culture for metabolic analysis; thus, information of spatial distribution is not preserved. In addition, the contribution from different cell types, each of which could have a very distinct metabolic profile, is lost. To fully

understand the role of metabolites and cell function, it is crucial not only to identify but also to correlate cellular metabolites in the context of tissue anatomy and cell-type composition.

Mass spectrometry imaging (MSI), an emerging technology, enables simultaneous *in situ* detection of individual molecular species of metabolites while preserving tissue morphology.^{19,20} In contrast to common molecular biology techniques, including chemical staining, immuno-based imaging approaches, and *in situ* hybridization, MSI does not require any prior knowledge of the target species and is completely label-free. Ambient MSI techniques,²¹ such as desorption electrospray ionization (DESI) MSI, have become increasingly used for biological tissue imaging as they allow analysis to be performed in the open environment with minimal sample preparation and is perfectly suitable for the analysis of small molecules.^{19,22–25} Besides DESI, secondary ion mass spectrometry (SIMS)^{26–28} and matrix-assisted laser desorption

Received: June 13, 2020

Accepted: September 3, 2020

Published: September 3, 2020



ionization (MALDI)^{29–31} are two major alternative sample ionization methods of MSI. Other varieties are also available.^{20,32,33} DESI, SIMS, and MALDI imaging technologies are complementary, and the choice of ionization method depends on the user's preferred requirements such as spatial resolution, m/z detection range, area to be imaged, the time required for sample preparation, data acquisition, and data analysis.²⁰

Importantly, MSI with cellular/subcellular resolution is an enormous challenge and remains a major driving force for making improvements in spatial resolution of MSI.^{34–39} Instrumentation advances allow SIMS and MALDI-MSI to achieve single-cell/subcellular spatial resolution,^{40–46} which enables cellular profiling of metabolites combining with fluorescence microscopy by antibody labeling.^{47–49} In contrast, DESI-MSI so far has not achieved spatially single-cell resolution, and therefore *in situ* cellular metabolic profiles could not be obtained. The lateral resolution of DESI-MSI can reach about 20 μm with optimal parameter settings, but the typical resolution is about 100–200 μm , which is determined by the effective surface area extracted by the spray solvent. Many efforts have been made to improve the resolution of DESI-MSI, including instrumental approaches such as the optimization of emitter capillary size, solvent composition, solvent flow rate, MS scan rate and step size,³⁹ and image fusion methods such as the fusion of DESI-MSI with optical microscopy of hematoxylin and eosin (H&E) staining to produce the improved molecular distribution in tissues.⁵⁰ To date, DESI-MSI cannot provide cell-type-specific information due to the inherent restriction of the DESI probe. Metabolic information obtained from one pixel of DESI-MSI can neither distinguish between variations in different cell types and frequencies nor identify the contributions of different cell types to the total measured metabolites. This prevents DESI-MSI being used for complex tissues with a number of mixed cell types in each individual DESI-MSI scan. To acquire the above information, experiments such as analysis of different types of cells from cell culture or cell sorting from isolated subsets of tissue might provide the solution.⁵¹ However, cellular structures such as neuronal axon and metabolic states can be compromised simultaneously during tissue dissociation and sorting, which may introduce bias in understanding cell-type-specific metabolism under physiological conditions. Despite its relatively restricted spatial resolution compared to other technologies, one of the defining features of DESI-MSI is its histologically compatible solvent system.^{19,25,52,53} The advantages that this capability brings are twofold: (1) it allows cell-type identification on the very same tissue section following an MSI scan, providing an unambiguous correlation between MS profiling and its corresponding region on each given tissue; and (2) all staining and imaging can be done postfix after the MSI procedure, so that it does not introduce any possible external interference between tissue sample collection and assessment.

In this study, we develop a powerful new chemical imaging capability in DESI-MSI that enables metabolic profiling of cell types in tissues. This is accomplished by combining DESI-MSI and immunofluorescence staining with specific cell-type markers, and the metabolic features of cell types are recognized by machine learning. We take advantage of the heterogeneity of the frequency of two main cell types (astrocytes and neurons) in the lateral septal nucleus of the mouse forebrain, which allows us to apply convex optimization—a machine learning method to computationally deconvolve the contribu-

ting metabolic profiles from astrocytes and neurons distinctively. The method provides a unique tool to study *in situ* cell-type-specific metabolic profiles in complex tissues with heterogeneous cell-type composition.

EXPERIMENTAL SECTION

DESI-MSI. A custom-built DESI imaging stage was coupled to a hybrid LTQ-Orbitrap mass spectrometer (Thermo Fisher Scientific) for DESI-MSI. The mass spectra were acquired in the negative ion mode from m/z 50–1000 using the Orbitrap as the mass analyzer with the resolving power set at 60 000. The spray voltage was set to -3.5 kV, and the capillary voltage was set to -65 V. The tube lens voltage was set to -120 V. Ion injection time was 100 ms, and one microscan was performed. The solvent system used is *N,N*-dimethylformamide (DMF)/acetonitrile (ACN) = 1:1 (vol/vol)⁵³ and provided at a flow rate of 0.8 $\mu\text{L}/\text{min}$. Assisted by a nebulizing gas (N_2) at a pressure of 150 psi, molecules of interest from tissues are desorbed and ionized. DESI spray tip-to-surface distance was 2 mm; spray incident angle was 56° , and spray-to-inlet distance was 6.5 μm . Step size in the moving stage was set to 200 μm , and automatic gain control of mass spectrometer was switched off. These parameters were empirically found to yield the optimal MS signal from brain tissues. All experiments were carried out under identical experimental conditions to allow a comparison between measurements.

Immunofluorescence Staining and Imaging. After each DESI scan, tissue sections were fixed with 4% paraformaldehyde (Electron Microscopy Science, Cat#15714) diluted in phosphate-buffered saline for 20 min at -20 $^\circ\text{C}$. Antibodies against the astrocyte marker Glial Fibrillary Acidic Protein (GFAP) antibody (Abcam, ab53554) were used at 1:1000 dilution at 4 $^\circ\text{C}$ overnight. Donkey antibody conjugated with Alexa Fluor 647 (Thermo Fisher Scientific, Cat# A-21447) was used at 1:250 dilution at room temperature for 1.5 h for a secondary staining. All sections were then mounted with 50 μL of ProLongTM Gold Antifade mounting media containing a fluorescent nucleic acid dye 4',6-diamidino-2-phenylindole (DAPI) (Thermo Fisher Scientific, P36931) before being imaged. Confocal microscopy was carried out using a Nikon Eclipse Ti confocal microscope equipped with a Zyla sCMOS camera (Andor) and NIS-Elements software (AR 4.30.02, 64-bit) using a 10 \times objective. No blinding was performed for taking pictures. The lateral septal nucleus region was defined using these anatomical landmarks shown on immunofluorescent images based on Allen Mouse Brain Atlas.^{54,55} Top: horizontal line immediately underneath the crossing of the bottom of corpus callosum with coronal section midline; bottom: 400 μm below top boundary; left and right: the left and right medial wall of the left and right lateral ventricle, respectively. A schematic figure showing the defined lateral septal nucleus region used in this study is represented in Figure 3a. The confocal images can be downloaded from MetaboLights at: <http://www.ebi.ac.uk/metabolights/MTBLS1747>.

Image Quantification. Image quantification was performed using a custom Julia language script. Briefly, for each immunofluorescence-stained region, nuclei were detected using DAPI and a blob detection algorithm provided by Images.jl. Using the immediate region including and surrounding the detected nuclei, cells were classified as either GFAP-positive (astrocytes) or GFAP-negative (likely neurons). Although neuron, oligodendrocytes, and microglia all

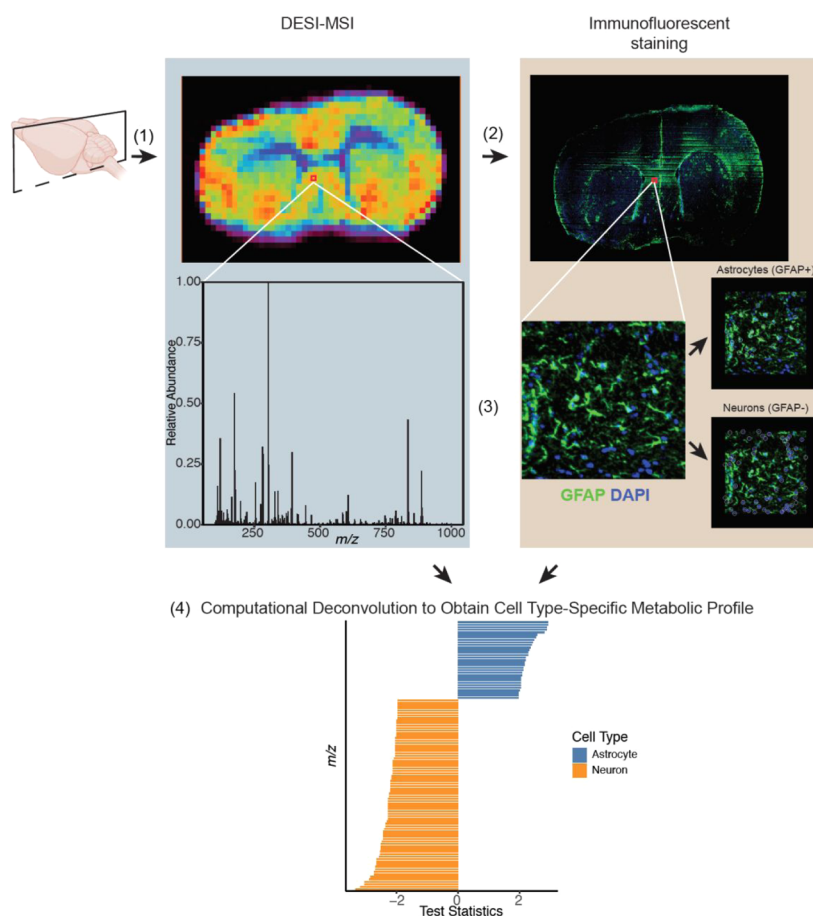


Figure 1. Schematic of the experimental design of the new chemical imaging capability that enables cell-type-specific metabolic profiling in a complex tissue. It was achieved by dual-modality imaging combined with machine learning: (1) DESI-MSI was performed on the coronal section of mouse brain; (2) after DESI-MSI, neurons and astrocytes were labeled by antibodies specifically; (3) MSI images were then overlaid with fluorescence images to obtain pixel information of metabolic distribution, cell number and cell types in the lateral septal nucleus region in the forebrain; (4) cell-type-specific metabolic profiles were then deconvolved by solving a convex optimization problem and features of signature metabolites could then be obtained by a statistical test.

exhibit negative GFAP staining, given the low level of mRNA expression detected from oligodendrocyte and microglia-specific marker genes in the lateral septal nucleus (Figure S2, and more in the Results and Discussion section),^{54,55} the vast majority of GFAP-negative cells that were identified in our current study in the lateral septal nucleus region are likely neurons. To this end, we used Otsu's method⁵⁶ to determine a threshold for summed intensity within a given region. Once cells were labeled based on summed GFAP intensity with respect to the threshold, each stained region was given a value for the percentage of astrocytes and neurons based on the ratio of these GFAP-positive and GFAP-negative cells to total detected cells, respectively (Table S1).

Machine Learning Approaches for Mass Spectra Deconvolution. The acquired raw data from Xcalibur were imported into BioMAP and MSiReader to obtain DESI-MS images and coregistered them with fluorescence images (see Supporting Information S3). Mass spectra from regions of interest as determined by immunofluorescence imaging were extracted and converted to text files. The raw mass spectra were first filtered by the frequency and relative intensity of the peaks. Peaks that only appear in less than two samples or peak intensities that were less than 0.1% of the maximum value were filtered out. The cell counts from the fluorescence image and the mass spectra were then combined to extract mass spectra

for different cell types. Ordinary least-squares methods are not suitable for this problem as the solutions may contain negative peak intensity values. Instead, we formulated this problem as a convex optimization, which can then be solved by convex solvers. Briefly, let $X \in \mathbb{R}^{n \times d}$ be the set of mass spectra obtained, where n is the number of samples, d is the number of distinct peaks in the mass spectra, and X_{ij} is the mass intensity of sample i at peak j ; $C \in \mathbb{R}^{n \times m}$ be the counting of the m kinds of cells in the n samples; and $M \in \mathbb{R}^{m \times d}$ be the mass spectra of the m kinds of cells we are solving for. The convex optimization problem was then formulated as

$$\begin{aligned} &\text{minimize} \quad \|CM - X\|_2^2 \\ &\text{subject to} \quad M \geq 0 \end{aligned}$$

where $\|\cdot\|_2$ stands for l_2 norm, and $M \geq 0$ represents M is elementwise greater than or equal to 0. The convex optimization problem was then solved by the open-source package of cvxpy.^{57,58} Note that this method is limited by the intrinsic properties of linear systems. For example, when all samples have the same ratio of one cell type to another, the matrix C becomes singular, and no unique solution exists. Therefore, the successful application of this procedure depends on the existence of a heterogeneous distribution of the cell types, which of course is the common situation. Representative

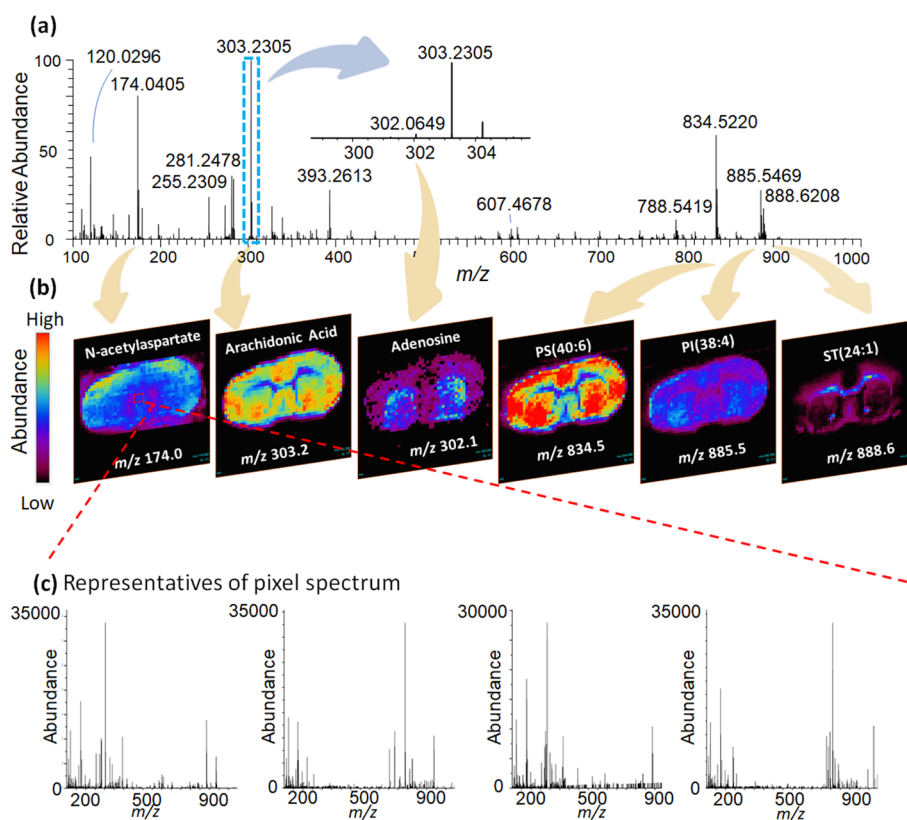


Figure 2. (a) Representative mass spectrum of mouse brain scanning using DESI-MSI. (b) Ion images of metabolites, *N*-acetylaspartate, arachidonic acid, PS (40:6), PI (38:4), and ST (24:1), showing different spatial distributions in mouse brain. Mass intensity was reduced by a factor of 2 for *N*-acetylaspartate and arachidonic acid and increased by a factor of 10 for adenosine to visualize using the same scale. (c) Representative mass spectra of pixels exacted from DESI-MSI, showing metabolic variation due to different cell number and cell types in each pixel. Each representative mass spectrum originates from different pixels.

pixel metabolic profiles (Figure S1) show the variety of cellular metabolites in each pixel. Other aspects that are required to apply this method are (1) the frequency at which the cells in the selected pixels are intermingled differs from pixel to pixel, allowing robust deconvolution; (2) the different cell types have very different metabolic characteristics (e.g., neurons and astrocytes); and (3) the number of cell types is relatively low (e.g., two types in this study) so as not to overcomplicate the solution. The method itself has no limit to the number of cell types as long as enough pixels are provided to generate a unique solution. The deconvolved spectra were visualized by mapping to a two-dimensional space using partial least square-discriminant analysis (PLS-DA), and the differences between metabolic distributions were tested by the Wilcoxon rank-sum test. We obtained 10 samples and extracted 10 pixels from each sample. The deconvolution was performed using the 10 pixels for each sample separately. Therefore, 10 deconvoluted spectra for each cell type were obtained, with each of them coming from a different sample. The 20 deconvoluted spectra were used in the Wilcoxon rank-sum test. The analysis was done using the package of scikit-learn.⁵⁹ All codes used for imaging analysis and cell-type-specific deconvolution by machine learning are available on GitHub repository for this paper (https://github.com/lightingghost/cell_type_mass_spec_imaging).

RESULTS AND DISCUSSION

Cell-Type-Specific Metabolite Measurement Using Dual-Modality Imaging Methods Combined with

Machine Learning. We performed differential metabolite analysis for two cell types, neurons and astrocytes, in mouse brain tissue *in situ* by dual-modality imaging combined with machine learning (Figure 1), which was illustrated by the following four steps: (1) Spatial distribution of metabolites of lateral septal nucleus in adult mouse forebrain was measured by DESI-MSI coupled to a mass spectrometer (Thermo LTQ Orbitrap XL) having both high mass resolution and tandem MS for structural analysis. A typical spatial resolution of DESI-MSI, 200 μm , was used; therefore, the total number of cells included in one scan pixel ranged from 48 to 156 cells. (2) After DESI-MSI experiments, cells were labeled by cell-type-specific antibodies. Neurons and astrocytes were identified, and the frequency of each cell type was quantified. (3) MSI images were then overlaid with fluorescence images to obtain pixel information of metabolic distribution, cell numbers, and cell types. Mass spectrum extracted from one MSI scan pixel reflects the composition of all of the cells in that pixel. Different MSI pixels include mixed cell types and different cell numbers, which leads to differences in the mass spectra of MSI pixels. (4) Cell-type-specific metabolic profiles were then deconvolved by solving a convex optimization problem, a machine learning method. This method relies on the variation in the frequency of different cell types in each given MSI pixel, which is an inherent nature for almost all complex tissue samples with mixed cell types. In our study, we focused on the lateral septal nucleus region in the forebrain, which is dominated by neurons and astrocytes. Details of our results in each step are elaborated in the following sections.

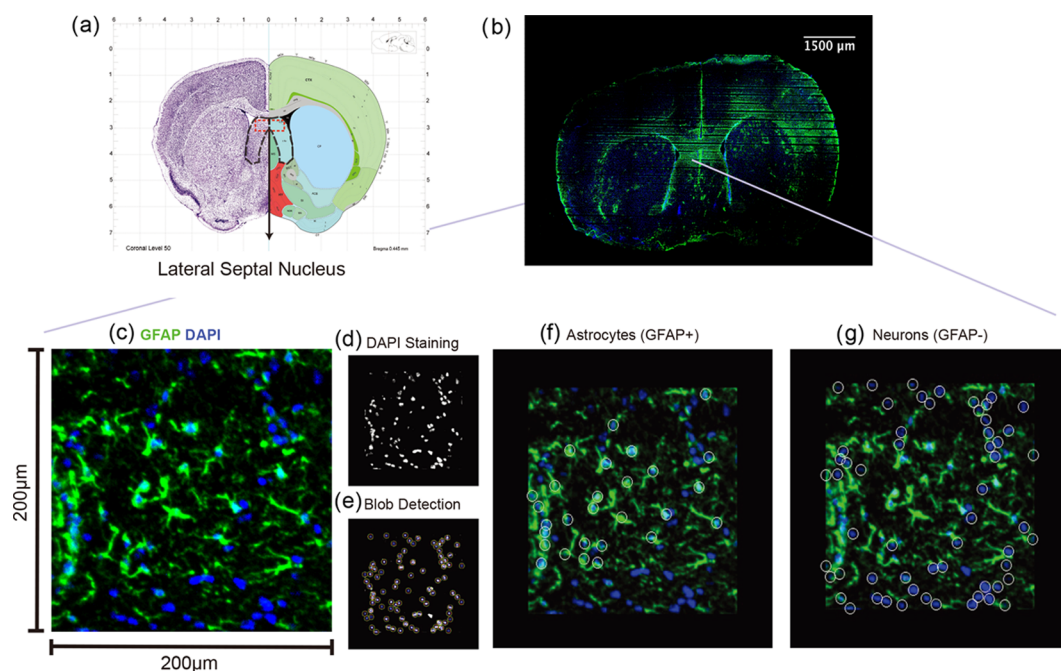


Figure 3. (a) Schematic showing the region of interest in this study. A rectangular area (red dashed rectangle) within the lateral septal nucleus region (black dashed symmetrical regions) in the coronal section (Bregma 0.445 mm) of mouse brain tissue, image obtained from Allen Developing Mouse Brain Atlas.^{54,55} (b) Fluorescence images of mouse brain tissue after cell labeling using GFAP antibody and DAPI. (c) Fluorescence images of one MSI pixel with a dimension of $200\ \mu\text{m} \times 200\ \mu\text{m}$ showing cell numbers and types using GFAP labeling in green and DAPI labeling in blue. (d) Image after DAPI staining. (e) Blob detection showing the total number of cells in one MSI pixel. (f) Fluorescence image with a gray circle showing the number of astrocytes in one MSI pixel. (g) Fluorescence image with gray circle showing the number of neurons in one MSI pixel.

Extraction of Pixel Mass Spectra from DESI-MSI Data.

DESI-MS imaging was carried out on coronal sections of 10 mouse brain samples. A histologically compatible solvent system, composed of *N,N*-dimethylformamide (DMF)/acetonitrile (1:1, vol/vol), was used in DESI-MSI experiments.⁵³ This method allowed immunofluorescence staining to be performed on the very same tissue section previously analyzed by DESI-MSI, which provides an unambiguous correlation between metabolic signatures and cell-type identity. Reproducibility was investigated by analyzing the same mouse brain tissue section on different days. Very small variations were found for MS peaks in the pixels (RSD = 8% when the cutoff value of the noise intensity was set at 0.005). The representative mass spectra of a pixel obtained from the DESI-MSI of the same tissue section on two different days are shown in Figure S5. The main metabolites observed in the examination of mouse brain tissues in the mass range of m/z 100–1000 (Figure 2a) were majorly amino acids, nucleosides, saturated and unsaturated fatty acids (FA), glycerophosphoinositols (PI), glycerophosphoserines (PS), glycerophosphethanolamines (PE), phosphatidic acid (PA), and sulfatides (ST). Representative images of metabolites including *N*-acetylaspargate (m/z 174.0), adenosine (m/z 302.1), arachidonic acid (m/z 303.2), PS (40:6) (m/z 834.5), PI (38:4) (m/z 885.5), and ST (24:1) (m/z 888.6) are shown in Figure 2b, and they present very different distributions in the brain sections. Metabolic profiling on neurons and astrocytes has always been of great interest in the field. MSI offers the possibility to provide new insights, whereas traditional MS technology relies heavily on mechanical dissociation of cells which is challenging due to intricate cellular structures, such as axon in neurons. In this study, we focus on lateral septal nucleus areas in the

forebrain because this region is demarcated with distinct anatomical landmarks on coronal section (Figures 3a and S2a).

Additionally, it contains a robust and heterogeneous distribution of GFAP-positive (likely astrocytes) and GFAP-negative (likely neurons) cells (Figures 1, S2b,c, and 3b). As a proof of principle effort to start delineating the cell-type-specific metabolic profiling in neurons and astrocytes, this provides an ideal setup for accurate data acquisition and downstream analysis. Functionally, the lateral septal nucleus also occupies one of the most strategically important positions in the forebrain; it is known to receive a reciprocal connection from the olfactory bulb, hippocampus, hypothalamus, and midbrain and play roles in critical physiological function in animals such as regulating social behavior, reward, and anxiety.^{60,61} So far, cell-type-specific metabolic study on neurons and astrocytes in septal areas is largely unexplored, which hinders our understanding of their functional roles. We extracted mass spectrometric information of metabolites from septal nucleus areas and displayed it in the forms of pixel mass spectra (Figure 2c). Ten pixels from each individual mouse were extracted from the overlay images of DESI-MSI and fluorescence images in lateral septal nucleus of the mouse forebrain. Due to different numbers of cells and cell types in each pixel, the metabolic profile varies from pixel to pixel. In total, 100 pixels from lateral septal nucleus were subjected to analysis.

Immunofluorescence Imaging of Neurons and Astrocytes. We took advantage of the fact that cellular structure and protein remain intact following the DESI-MSI scan. This enables us to use the very same tissue section that has been subjected to DESI-MSI for cell-type identification and quantification using immunofluorescence staining. Brain

sections were stained with an antibody against astrocyte-specific marker Glial Fibrillary Acidic Protein (GFAP). We also applied a commonly used fluorescent nucleic acid dye 4',6-diamidino-2-phenylindole (DAPI) to identify the nucleus of each cell. Following confocal fluorescence microscopy, we quantified the total number of intact cells using blob detection (see the **Image Quantification** section above for more details) on areas that are positively stained with DAPI in each pixel. Using the immediate region including and surrounding the detected nuclei, cells were then classified as either GFAP-positive (likely astrocytes) or GFAP-negative (likely neurons) using Otsu's method.⁵⁶

While astrocyte marker GFAP can also label neural stem cells in neurogenic regions of mouse brain, such as the subventricular zone and the hippocampal dentate gyrus, to our knowledge, cells that are positively labeled by GFAP in the lateral septal nucleus region should almost exclusively be astrocytes.⁶² Neuron, oligodendrocyte, and microglia are the other three differentiated cell types in the adult brain besides astrocyte, all of which exhibit negative GFAP staining. Given the low level of mRNA expression detected by *in situ* hybridization^{54,55} of myelin basic protein (*Mbp*) (an oligodendrocyte marker) (Figure S2d) or allograft inflammatory factor 1 (*Aif1*, also known as *Iba1*) (a microglia marker) (Figure S2e) in the lateral septal nucleus,⁶³ the vast majority of GFAP-negative cells that were identified in our current study in the lateral septal nucleus region are likely neurons. However, even with very low levels of oligodendrocyte present, we cannot entirely exclude the possibility that myelin sheaths, which are generated by oligodendrocytes and wrap around neuronal axons, are being captured in the lateral septal nucleus region. Once cells were characterized as either GFAP-positive astrocytes or GFAP-negative neurons, the frequency of each of these two cell types was quantified in all 100 pixels for downstream computational analysis and metabolic profile deconvolution.

Metabolic Profiling of Neurons and Astrocytes. By overlaying MSI scans with immunofluorescence images, metabolic profiles from each matching MSI pixels in lateral septal nucleus were extracted. Given the 200 μm diameter of the spray spot, variations of metabolites in mass spectrum obtained from each pixel could be due to the differences in cellular metabolic states or cell-type composition in different pixels of the tissue. With the cell-type frequency quantification of neuron and astrocyte from each pixel, we were then able to apply convex optimization in all samples, which provided us the cell-type-specific metabolic profiles of astrocyte (Figure 4a) and neuron (Figure 4b) from all samples. Metabolites ranging from m/z 100 to 1000 show distinct patterns in astrocytes and neurons.

To visualize the variation and separation of the deconvolved metabolic profiles from neurons and astrocytes, we performed partial least-squares-discriminant analysis (PLS-DA) using all 4450 detected metabolic features from mass spectra. Computationally, deconvolved metabolic profile of neurons and astrocytes from all samples were clustered into two populations based on their cell-type identification (Figure 5), suggesting very distinct and reproducible metabolic signatures between these two cell types. The Wilcoxon rank-sum test reveals that 107 metabolites show statistically distinct abundance between two cell types (Figure 6a), with 31 metabolites displaying enriched intensity in astrocytes and 76 showing accumulation in neurons (Figures 6b and S3). Molecular compound

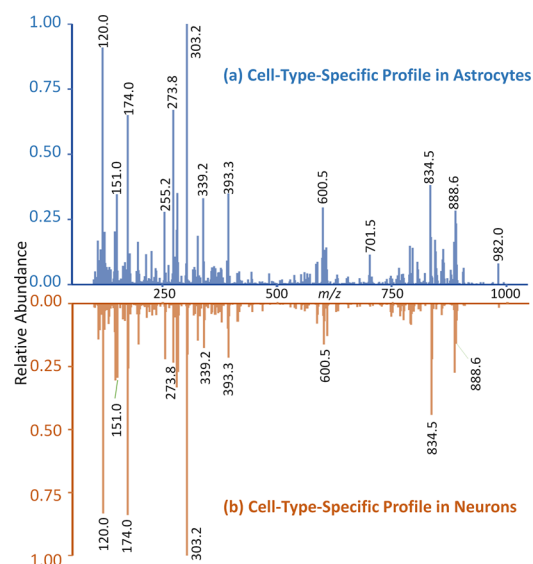


Figure 4. Cell-type-specific metabolic profile in (a) astrocytes; (b) neurons obtained by convex optimization of cell-type frequency quantification of neurons and astrocytes from 100 pixels in the lateral septal nucleus region of 10 different mouse brain tissues.

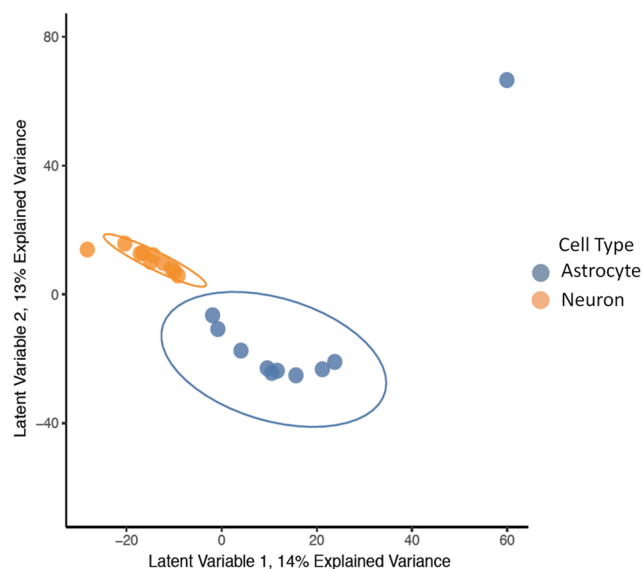


Figure 5. Visualization of partial least-squares-discriminant analysis using 4450 detected metabolite features in astrocytes and neurons, showing cells were clustered into two populations, which suggests very distinct and reproducible metabolic signatures between these two cell types. Each dot represents one type of cells from an individual mouse brain. Mass spectra of 10 pixels were obtained for each individual mouse brain. The circle around each cluster represents a data ellipse drawn at a 95% level. The outlier may come from the heterogeneity of different samples.

characterization was then performed using high-resolution MS and tandem MS, and 23 distinct metabolites (Table S1) were identified. Interestingly, adenosine is highly enriched in astrocytes as compared to neurons (Figure 2b and Table S1). This is consistent with previous reports showing a higher level of adenosine uptake by astrocytes compared to neurons⁶⁴ and a key role of astrocytes in regulating synaptic levels of adenosine, which is important for synaptic plasticity.^{65–67} On the other hand, we observed that *N*-acetylaspartate (NAA) is

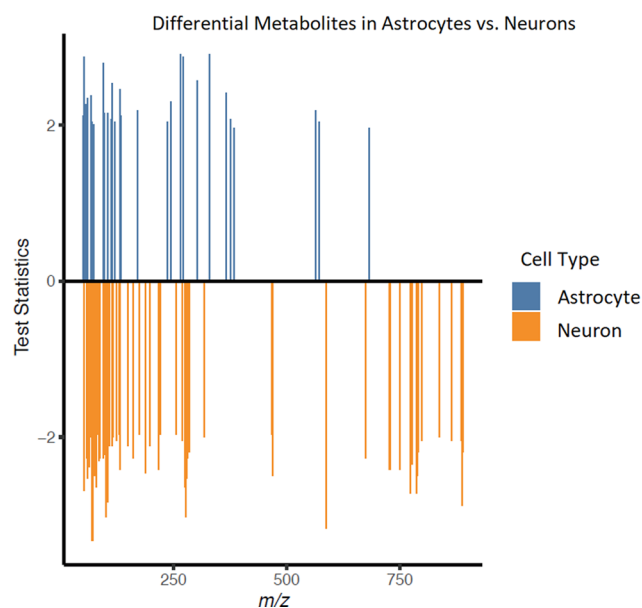


Figure 6. Result of Wilcoxon's rank-sum test revealing that 107 metabolites show statistically distinct abundance between astrocytes and neurons in the lateral septal nucleus region of mouse brain tissue, with 31 metabolites displaying enriched intensity in astrocytes and 76 showing accumulation in neurons (The m/z values of 107 featured metabolites and the annotations of identified metabolites are shown in Figure S3).

significantly more abundant in neurons than astrocytes (Figure 2b and Table S1). NAA is a metabolite specific to the nervous system, which is synthesized in neurons.⁶⁸ Importantly, previous studies indicated that NAA shows a high concentration in medial and lateral septal nucleus, which we were able to corroborate in the metabolic profile of neurons from the same region. Thus, our identification of metabolites such as adenosine and NAA, which were previously associated with astrocytes and neurons, respectively, provides validation for our experimental and *in silico* pipeline.

We also made novel observations: for example, we observed a list of phospholipids that are significantly more abundant in neurons than astrocytes, such as lipids in classes of PE, PA, PG, PI, PS, and sulfatide (Table S1). Besides previous report suggesting an overall higher level of lipid turnover in neurons compared to astrocytes, how individual phospholipid could be differentially regulated between these two cell types are largely unexplored.⁶⁹ PE, PG, PI, PS, and sulfatide are major membrane components that can become building blocks of the plasma membrane as well as a variety of organelle membranes. Interestingly, phospholipid composition has been implicated in regulating important neuronal functions such as synaptic vesicle fusion and receptor accessibility,⁷⁰ which could potentially contribute to the relative abundance of these phospholipids in neurons. Moreover, given that the astrocytes in septal nuclei are mostly fibrous astrocytes, which are known to have very sparse organelles than neurons,^{71,72} the difference in phospholipid intensity might be caused by distinct organelle composition in neurons and astrocytes.

CONCLUSIONS

Complex tissue samples with mixed cell populations present a challenge in determining the metabolic profiles of different cell types. We present a method that integrates the rich chemical

information found within mass spectra recorded by DESI-MSI, with the well-defined cellular classifications obtained by immunochemical staining from thousands of cells. Downstream machine learning enables computational deconvolution. Based on this method, we report cell-type-specific metabolic profiles from neurons and astrocytes in the lateral septal nucleus of the adult mouse forebrain. Featured metabolites such as adenosine and *N*-acetylaspartate are in line with our current understanding of their functions in astrocytes and neurons, respectively. Excitingly, our method also reveals the accumulation of phospholipid species from a few different classes in neurons that could provide new opportunities for future functional metabolic studies between these two important cell types—neurons and astrocytes—in the central nervous system. Our method can infer the spectra of distinct cell types in a mixture when we know the spectrum of the mixture and the percentage of each cell type. Conversely, this method could also be used to infer the percentage of each component when we know the spectrum of the mixture and the spectra of different components, and thereby could reveal cellular heterogeneity in a tissue. For example, many studies have shown that cancer cells have distinct metabolic profiles from normal cells.^{73,74} We envision this method could be applied to obtain the metabolic profiles of cancer cells vs normal cells, especially for tumors that have cancer cells sparsely distributed throughout normal cells. Thus, this method should allow several applications in cellular metabolomics in samples with heterogeneous cell types, provided that there are enough differences between the cell types.

ASSOCIATED CONTENT

Supporting Information

The Supporting Information is available free of charge at <https://pubs.acs.org/doi/10.1021/acs.analchem.0c02519>.

Metabolic profiles of pixels; cell-type-specific marker gene visualization; identified metabolites; and Wilcoxon's rank-sum test result (Figures S1–S3 and Table S1) (PDF)

AUTHOR INFORMATION

Corresponding Authors

Anne Brunet – Department of Genetics and Glenn Laboratories for the Biology of Aging, Stanford University, Stanford, California 94305, United States; Email: anne.brunet@stanford.edu

Richard N. Zare – Department of Chemistry, Stanford University, Stanford, California 94305, United States; orcid.org/0000-0001-5266-4253; Email: rnz@stanford.edu

Authors

Xin Yan – Department of Chemistry, Texas A&M University, College Station, Texas 77843, United States; Department of Chemistry, Stanford University, Stanford, California 94305, United States

Xiaoai Zhao – Department of Genetics, Stanford University, Stanford, California 94305, United States

Zhenpeng Zhou – Department of Chemistry, Stanford University, Stanford, California 94305, United States

Andrew McKay – Department of Genetics, Stanford University, Stanford, California 94305, United States

Complete contact information is available at:

<https://pubs.acs.org/10.1021/acs.analchem.0c02519>

Author Contributions

X.Y., X.Z., and Z.Z. contributed equally. X.Y., X.Z., Z.Z., A.B., and R.N.Z. planned the study. X.Y. performed DESI-MSI acquisition. X.Z. performed experimental sample preparation and immunofluorescent staining and microscopy. Z.Z. performed convex optimization and statistical analysis. A.M. performed image quantification. X.Y., X.Z., and Z.Z. wrote the manuscript with help from R.N.Z. and A.B. All authors discussed the results and commented on the manuscript.

Notes

The authors declare no competing financial interest.

ACKNOWLEDGMENTS

This work was funded by the Air Force Office of Scientific Research through Basic Research Initiative Grant AFOSR FA9550-16-1-0113 (R.N.Z.), the National Science Foundation under the Data-Driven Discovery Science in Chemistry (D3SC) for Early Concept Grants for Exploratory Research (EAGER Grant CHE-1734082 to R.N.Z.), and National Institute of Health (R01AG056290 and P01AG036695 to A.B.).

REFERENCES

- (1) Oldiges, M.; Lütz, S.; Pflug, S.; Schroer, K.; Stein, N.; Wiendahl, C. *Appl. Microbiol. Biotechnol.* **2007**, *76*, 495–511.
- (2) Mutlu, A. S.; Gao, S. M.; Zhang, H.; Wang, M. C. *Nat. Commun.* **2020**, *11*, No. 1450.
- (3) Neve, I. A. A.; Sowa, J. N.; Lin, C. J.; Sivaramakrishnan, P.; Herman, C.; Ye, Y.; Han, L.; Wang, M. C. *G3* **2020**, *10*, 189–198.
- (4) Dettmer, K.; Aronov, P. A.; Hammock, B. D. *Mass Spectrom. Rev.* **2007**, *26*, 51–78.
- (5) Liesenfeld, D. B.; Habermann, N.; Owen, R. W.; Scalbert, A.; Ulrich, C. M. *Cancer Epidemiol. Biomarkers Prev.* **2013**, *22*, 2182.
- (6) Roux, A.; Lison, D.; Junot, C.; Heilier, J.-F. *Clin. Biochem.* **2011**, *44*, 119–135.
- (7) Madsen, R.; Lundstedt, T.; Trygg, J. *Anal. Chim. Acta* **2010**, *659*, 23–33.
- (8) Beger, R. D. *Metabolites* **2013**, *3*, 552–574.
- (9) Armitage, E. G.; Barbas, C. J. *Pharm. Biomed. Anal.* **2014**, *87*, 1–11.
- (10) Ma, Y.; Zhang, P.; Yang, Y.; Wang, F.; Qin, H. *Mol. Biol. Rep.* **2012**, *39*, 7505–7511.
- (11) Ussher, J. R.; Elmariah, S.; Gerszten, R. E.; Dyck, J. R. B. *J. Am. Coll. Cardiol.* **2016**, *68*, 2850–2870.
- (12) Cheng, S. S.; Shah, S. H.; Corwin, E. J.; Fiehn, O.; Fitzgerald, R. L.; Gerszten, R. E.; Illig, T.; Rhee, E. P.; Srinivas, P. R.; Wang, T. J.; Jain, M.; American Heart Association Council on Functional Genomics and Translational Biology; Council on Cardiovascular and Stroke Nursing; Council on Clinical Cardiology; and Stroke Council. *Circ. Cardiovasc. Genet.* **2017**, *10*, No. e000032.
- (13) Jové, M.; Portero-Otin, M.; Naudi, A.; Ferrer, I.; Pamplona, R. *J. Neuropathol. Exp. Neurol.* **2014**, *73*, 640–657.
- (14) Botas, A.; Campbell, H. M.; Han, X.; Maletic-Savatic, M. *Int. Rev. Neurobiol.* **2015**, *122*, 53–80.
- (15) Ibanez, C.; Cifuentes, A.; Simo, C. *Int. Rev. Neurobiol.* **2015**, *122*, 95–132.
- (16) Suhre, K.; Meisinger, C.; Doring, A.; Altmaier, E.; Belcredi, P.; Gieger, C.; Chang, D.; Milburn, M. V.; Gall, W. E.; Weinberger, K. M.; Mewes, H. W.; de Angelis, M. H.; Wichmann, H. E.; Kronenberg, F.; Adamski, J.; Illig, T. *PLoS One* **2010**, *5*, No. e13953.
- (17) Guasch-Ferré, M.; Hruby, A.; Toledo, E.; Clish, C. B.; Martinez-Gonzalez, M. A.; Salas-Salvado, J.; Hu, F. B. *Diabetes Care* **2016**, *39*, 833–846.
- (18) Rauschert, S.; Uhl, O.; Koletzko, B.; Hellmuth, C. *Ann. Nutr. Metab.* **2014**, *64*, 314–324.
- (19) Wu, C. P.; Dill, A. L.; Eberlin, L. S.; Cooks, R. G.; Ifa, D. R. *Mass Spectrom. Rev.* **2013**, *32*, 218–243.
- (20) Buchberger, A. R.; DeLaney, K.; Johnson, J.; Li, L. J. *Anal. Chem.* **2018**, *90*, 240–265.
- (21) Feider, C. L.; Krieger, A.; DeHoog, R. J.; Eberlin, L. S. *Anal. Chem.* **2019**, *91*, 4266–4290.
- (22) Wiseman, J. M.; Ifa, D. R.; Song, Q. Y.; Cooks, R. G. *Angew. Chem., Int. Ed.* **2006**, *45*, 7188–7192.
- (23) Ifa, D. R.; Wiseman, J. M.; Song, Q. Y.; Cooks, R. G. *Int. J. Mass Spectrom.* **2007**, *259*, 8–15.
- (24) Wiseman, J. M.; Ifa, D. R.; Venter, A.; Cooks, R. G. *Nat. Protoc.* **2008**, *3*, 517–524.
- (25) DeHoog, R. J.; Zhang, J.; Alore, E.; Lin, J. Q.; Yu, W.; Woody, S.; Almendariz, C.; Lin, M.; Engelsman, A. F.; Sidhu, S. B.; Tibshirani, R.; Suliburk, J.; Eberlin, L. S. *Proc. Natl. Acad. Sci. U.S.A.* **2019**, *116*, 21401–21408.
- (26) Brunelle, A.; Touboul, D.; Laprevote, O. *J. Mass Spectrom.* **2005**, *40*, 985–999.
- (27) Boxer, S. G.; Kraft, M. L.; Weber, P. K. *Annu. Rev. Biophys.* **2009**, *38*, 53–74.
- (28) Passarelli, M. K.; Winograd, N. *Biochim. Biophys. Acta* **2011**, *1811*, 976–990.
- (29) Hsieh, Y.; Casale, R.; Fukuda, E.; Chen, J. W.; Knemeyer, I.; Wingate, J.; Morrison, R.; Korfmacher, W. *Rapid Commun. Mass Spectrom.* **2006**, *20*, 965–972.
- (30) Schober, Y.; Guenther, S.; Spengler, B.; Rompp, A. *Anal. Chem.* **2012**, *84*, 6293–6297.
- (31) Norris, J. L.; Caprioli, R. M. *Chem. Rev.* **2013**, *113*, 2309–2342.
- (32) Chen, S.; Xiong, C.; Liu, H.; Wan, Q.; Hou, J.; He, Q.; Badu-Tawiah, A.; Nie, Z. *Nat. Nanotechnol.* **2015**, *10*, 176–182.
- (33) Roach, P. J.; Laskin, J.; Laskin, A. *Anal. Chem.* **2010**, *82*, 7979–7986.
- (34) Yang, J. H.; Caprioli, R. M. *Anal. Chem.* **2011**, *83*, 5728–5734.
- (35) Thomas, A.; Charbonneau, J. L.; Fournaise, E.; Chaurand, P. *Anal. Chem.* **2012**, *84*, 2048–2054.
- (36) Römpp, A.; Spengler, B. *Histochem. Cell Biol.* **2013**, *139*, 759–783.
- (37) Kompauer, M.; Heiles, S.; Spengler, B. *Nat. Methods* **2017**, *14*, 90–96.
- (38) Altelaar, A. F. M.; van Minnen, J.; Jimenez, C. R.; Heeren, R. M. A.; Piersma, S. R. *Anal. Chem.* **2005**, *77*, 735–741.
- (39) Kertesz, V.; Van Berkel, G. J. *Rapid Commun. Mass Spectrom.* **2008**, *22*, 2639–2644.
- (40) Zavalin, A.; Todd, E. M.; Rawhouser, P. D.; Yang, J. H.; Norris, J. L.; Caprioli, R. M. *J. Mass Spectrom.* **2012**, *47*, 1473–1481.
- (41) Dueñas, M. E.; Essner, J. J.; Lee, Y. J. *Sci. Rep.* **2017**, *7*, No. 14946.
- (42) Boggio, K. J.; Obasuyi, E.; Sugino, K.; Nelson, S. B.; Agar, N. Y. R.; Agar, J. N. *Expert Rev. Proteomics* **2011**, *8*, 591–604.
- (43) Nygren, H.; Hagenhoff, B.; Malmberg, P.; Nilsson, M.; Richter, K. *Microsc. Res. Tech.* **2007**, *70*, 969–974.
- (44) Heien, M. L.; Piehowski, P. D.; Winograd, N.; Ewing, A. G. *Methods Mol. Biol.* **2010**, *656*, 85–97.
- (45) Chandra, S.; Morrison, G. H. *Int. J. Mass Spectrom. Ion Processes* **1995**, *143*, 161–176.
- (46) Chandra, S. *Appl. Surf. Sci.* **2004**, *231–232*, 467–469.
- (47) Neumann, E. K.; Comi, T. J.; Rubakhin, S. S.; Sweedler, J. V. *Angew. Chem., Int. Ed.* **2019**, *58*, 5910–5914.
- (48) Lau, K. H.; Christlieb, M.; Schroder, M.; Sheldon, H.; Harris, A. L.; Grovenor, C. R. M. *J. Microsc.* **2010**, *240*, 21–31.
- (49) Kaya, I.; Michno, W.; Brinet, D.; Iacone, Y.; Zanni, G.; Blennow, K.; Zetterberg, H.; Hanrieder, J. *Anal. Chem.* **2017**, *89*, 4685–4694.
- (50) Lin, L. E.; Chen, C. L.; Huang, Y. C.; Chung, H. H.; Lin, C. W.; Chen, K. C.; Peng, Y. J.; Ding, S. T.; Wang, M. Y.; Shen, T. L.; Hsu, C. C. *Anal. Chim. Acta* **2020**, *1100*, 75–87.

- (51) Weaver, E. M.; Hummon, A. B. *Adv. Drug Delivery Rev.* **2013**, *65*, 1039–1055.
- (52) Garza, K. Y.; Feider, C. L.; Klein, D. R.; Rosenberg, J. A.; Brodbelt, J. S.; Eberlin, L. S. *Anal. Chem.* **2018**, *90*, 7785–7789.
- (53) Eberlin, L. S.; Ferreira, C. R.; Dill, A. L.; Ifa, D. R.; Cheng, L.; Cooks, R. G. *ChemBioChem* **2011**, *12*, 2129–2132.
- (54) Lein, E. S.; Hawrylycz, M. J.; Ao, N.; Ayres, M.; Bensinger, A.; Bernard, A.; Boe, A. F.; Boguski, M. S.; Brockway, K. S.; Byrnes, E. J.; Chen, L.; Chen, L.; Chen, T.-M.; Chi Chin, M.; Chong, J.; Crook, B. E.; Czaplinska, A.; Dang, C. N.; Datta, S.; Dee, N. R.; Desaki, A. L.; Desta, T.; Diep, E.; Dolbeare, T. A.; Donelan, M. J.; Dong, H.-W.; Dougherty, J. G.; Duncan, B. J.; Ebbert, A. J.; Eichele, G.; Estin, L. K.; Faber, C.; Facer, B. A.; Fields, R.; Fischer, S. R.; Fliss, T. P.; Frensley, C.; Gates, S. N.; Glattfelder, K. J.; Halverson, K. R.; Hart, M. R.; Hohmann, J. G.; Howell, M. P.; Jeung, D. P.; Johnson, R. A.; Karr, P. T.; Kawal, R.; Kidney, J. M.; Knapik, R. H.; Kuan, C. L.; Lake, J. H.; Laramée, A. R.; Larsen, K. D.; Lau, C.; Lemon, T. A.; Liang, A. J.; Liu, Y.; Luong, L. T.; Michaels, J.; Morgan, J. J.; Morgan, R. J.; Mortrud, M. T.; Mosqueda, N. F.; Ng, L. L.; Ng, R.; Orta, G. J.; Overly, C. C.; Pak, T. H.; Parry, S. E.; Pathak, S. D.; Pearson, O. C.; Puchalski, R. B.; Riley, Z. L.; Rockett, H. R.; Rowland, S. A.; Royall, J. J.; Ruiz, M. J.; Sarno, N. R.; Schaffnit, K.; Shapovalova, N. V.; Sivisay, T.; Slaughterbeck, C. R.; Smith, S. C.; Smith, K. A.; Smith, B. I.; Sodt, A. J.; Stewart, N. N.; Stumpf, K.-R.; Sunkin, S. M.; Sutram, M.; Tam, A.; Teemer, C. D.; Thaller, C.; Thompson, C. L.; Varnam, L. R.; Visel, A.; Whitlock, R. M.; Wohnoutka, P. E.; Wolkey, C. K.; Wong, V. Y.; Wood, M.; Yaylaoglu, M. B.; Young, R. C.; Youngstrom, B. L.; Feng Yuan, X.; Zhang, B.; Zwingman, T. A.; Jones, A. R. *Nature* **2007**, *445*, 168–176.
- (55) Dong, H. W. *The Allen Reference Atlas: A Digital Color Brain Atlas of the C57Bl/6J Male Mouse*; John Wiley & Sons Inc.: Hoboken, NJ, 2008; p 366.
- (56) Otsu, N. *IEEE Trans. Syst., Man, Cybern.* **1979**, *9*, 62–66.
- (57) Agrawal, A.; Verschuere, R.; Diamond, S.; Boyd, S. J. *Control Decis.* **2018**, *5*, 42–60.
- (58) Diamond, S.; Boyd, S. J. *Mach. Learn. Res.* **2016**, *17*, 2909–2913.
- (59) Pedregosa, F.; Varoquaux, G.; Gramfort, A.; Michel, V.; Thirion, B.; Grisel, O.; Blondel, M.; Prettenhofer, P.; Weiss, R.; Dubourg, V. *J. Mach. Learn. Res.* **2011**, *12*, 2825–2830.
- (60) Risold, P. Y.; Swanson, L. W. *Brain Res. Rev.* **1997**, *24*, 91–113.
- (61) Risold, P. Y.; Swanson, L. W. *Brain Res. Rev.* **1997**, *24*, 115–195.
- (62) Tatsumi, K.; Isonishi, A.; Yamasaki, M.; Kawabe, Y.; Morita-Takemura, S.; Nakahara, K.; Terada, Y.; Shinjo, T.; Okuda, H.; Tanaka, T.; Wanaka, A. *Front. Neuroanat.* **2018**, *12*, No. 8.
- (63) Gokce, O.; Stanley, G. M.; Treutlein, B.; Neff, N. F.; Camp, J. G.; Malenka, R. C.; Rothwell, P. E.; Fuccillo, M. V.; Südhof, T. C.; Quake, S. R. *Cell Rep.* **2016**, *16*, 1126–1137.
- (64) Hertz, L. J. *Neurochem.* **1978**, *31*, 55–62.
- (65) Boison, D.; Chen, J. F.; Fredholm, B. B. *Cell Death Differ.* **2010**, *17*, 1071–1082.
- (66) Pascual, O.; Casper, K. B.; Kubera, C.; Zhang, J.; Revilla-Sanchez, R.; Sul, J.-Y.; Takano, H.; Moss, S. J.; McCarthy, K.; Haydon, P. G. *Science* **2005**, *310*, 113–116.
- (67) Schubert, P.; Rudolph, K. A.; Fredholm, B. B.; Yoichi, N. *Int. J. Biochem.* **1994**, *26*, 1227–1236.
- (68) Moffett, J. R.; Namboodiri, M. A. A. *J. Neurocytol.* **1995**, *24*, 409–433.
- (69) Arienti, G.; Goracci, G.; Porcellati, G. *Neurochem. Res.* **1981**, *6*, 729–742.
- (70) Barber, C. N.; Raben, D. M. *Front. Cell. Neurosci.* **2019**, *13*, No. 212.
- (71) Haim, L. B.; Rowitch, D. H. *Nat. Rev. Neurosci.* **2017**, *18*, 31–41.
- (72) Miller, R. H.; Raff, M. C. *J. Neurosci.* **1984**, *4*, 585–592.
- (73) Griffin, J.; Shockcor, J. *Nat. Rev. Cancer* **2004**, *4*, 551–561.
- (74) Zhang, J.; Li, S. Q.; Lin, J. Q.; Yu, W.; Eberlin, L. S. *Cancer Res.* **2020**, *80*, 689–698.